Eur. Phys. J. Special Topics **226**, 2457–2475 (2017)

DOI: 10.1140/epjst/e2017-70059-7

THE EUROPEAN PHYSICAL JOURNAL SPECIAL TOPICS

Review

Influence of oxygen vacancies on two-dimensional electron systems at $SrTiO_3$-based interfaces and surfaces

Michael Sing[1], Harald O. Jeschke[2,a], Frank Lechermann[3,4], Roser Valentí[2,b], and Ralph Claessen[1]

[1] Physikalisches Institut and Röntgen Center for Complex Material Systems (RCCM), Universität Würzburg, 97074 Würzburg, Germany
[2] Institut für Theoretische Physik, Goethe-Universtät Frankfurt, 60438 Frankfurt am Main, Germany
[3] I. Institut für Theoretische Physik, Universität Hamburg, 20355 Hamburg, Germany
[4] Institut für Keramische Hochleistungswerkstoffe, Technische Universität Hamburg-Harburg, 21073 Hamburg, Germany

Received 17 February 2017 / Received in final form 13 March 2017
Published online 10 July 2017

Abstract. The insulator $SrTiO_3$ can host high-mobility two-dimensional electron systems on its surfaces and at interfaces with other oxides. While for the bare surface a two-dimensional electron system can only be induced by oxygen vacancies, it is believed that the metallicity of heterostructure interfaces as in $LaAlO_3/SrTiO_3$ is caused by other mechanisms related to the polar discontinuity at the interface. Based on calculations using density functional and dynamical mean-field theory as well as on experimental results using photoemission spectroscopy we elucidate the role of oxygen vacancies, thereby highlighting their importance for the electronic and magnetic properties of the systems under study.

1 Introduction

Already for a long time the physics of semiconductors and in particular their technological application relies on the exploitation of electronically active defects — electron donors and acceptors — that are implemented in the host materials usually in form of elemental impurities. Of paramount importance for the fabrication of working devices like metal oxide semiconductor field-effect transistors is the exact control over the spatially inhomogeneous distribution of these impurities at interfaces.

In the field of transition metal oxides defects are often unwanted since they cause disorder which often does harm to or even completely destroys the intrinsic functionalities of oxides such as superconductivity or magnetic order. An exception in some

[a] *Present Address*: Research Institute for Interdisciplinary Science, Okayama University, Okayama 700-8530, Japan
[b] e-mail: valenti@th.physik.uni-frankfurt.de

particular cases e.g., in high-T_c superconductors represents the oxygen stoichiometry because via the oxygen concentration the charge carrier doping can be tuned to ensure the highest T_c.

With the advent of modern thin film technology it became possible during the last one and a half decade to grow layered structures of transition metal oxides with a precision down to the atomic scale similar to what has been accomplished for many years for semiconductors on an industrial level. Thus the targeted manipulation and control of defects in oxides and in particular at their surfaces and interfaces open new avenues from both a fundamental and an applicational point of view.

A paradigmatic example for this development is the famous $LaAlO_3/SrTiO_3$ heterostructure. It develops a two-dimensional electron system with intriguing properties such as superconductivity or a dichotomy of superconductivity and magnetism at its interface but only if 4 or more monolayers of $LaAlO_3$ are grown on a properly prepared, TiO_2 terminated substrate. The question whether the interplay of film and substrate is decisive for the formation and the properties of this two-dimensional electron system or the substrate alone is sufficient to host two-dimensional conductivity of essentially the same kind has fuelled a vast number of experimental and theoretical studies.

In this review we cover both advanced theoretical and experimental methods which allow to investigate the influence of oxygen vacancies on two-dimensional electron systems at $SrTiO_3$-based interfaces and surfaces and summarize the relevant results.

2 Oxygen vacancies and surface two-dimensional electron systems in $SrTiO_3$

2.1 Oxygen-vacancy-induced localized versus itinerant states

The role of oxygen vacancies in the formation of the two-dimensional electron system (2DES) in $SrTiO_3$ has been a subject of intensive discussion in recent years both experimentally and theoretically [1–4]. A deep insight on the electronic behavior of oxygen-deficient $SrTiO_3$ surfaces can be gained from electronic structure calculations on $SrTiO_3$ slabs based on density functional theory (DFT). Here, we review results obtained by considering different $SrTiO_3$ slabs with various oxygen vacancy configurations and provide a comprehensive description of the origin of (i) the itinerant 2D electron system, (ii) the localized in-gap states, (iii) possible Rashba spin-orbit coupling and magnetism and (iv) possible oxygen clustering.

The series of investigated slabs both, SrO-terminated and TiO_2-terminated, are given in references [5–7]. In this article, we focus on representative examples of slabs with TiO_2 termination. In Figure 1 we show the cases of a TiO_2 terminated $2 \times 2 \times 6$ slab with a single oxygen vancancy in the surface layer (Fig. 1a) and a TiO_2 terminated $3 \times 3 \times 4$ slab with two vacancies in the surface layer (Fig. 1b). All slabs have a vacuum of at least 20 Å to avoid spurious interactions between the periodic images. In order to account for possible surface reconstruction, the internal coordinates of the slabs were relaxed with the projector-augmented wave basis [8] as implemented in the VASP [9,10] code. As exchange-correlation functional we employed the generalized-gradient approximation (GGA) [11] in the Dudarev scheme (GGA + U) [12,13]. The electronic structure was analyzed with the all-electron full-potential local orbital (FPLO) method [14]. GGA+U with $U = 5\,\text{eV}$ and $J_H = 0.64\,\text{eV}$ was performed using the atomic limit double counting correction.

The one-vacancy slabs provide already very valuable information on the formation of the 2DES. There is a significant surface reconstruction after introducing the oxygen vacancy and we found the formation of a metallic state only after the insertion of the

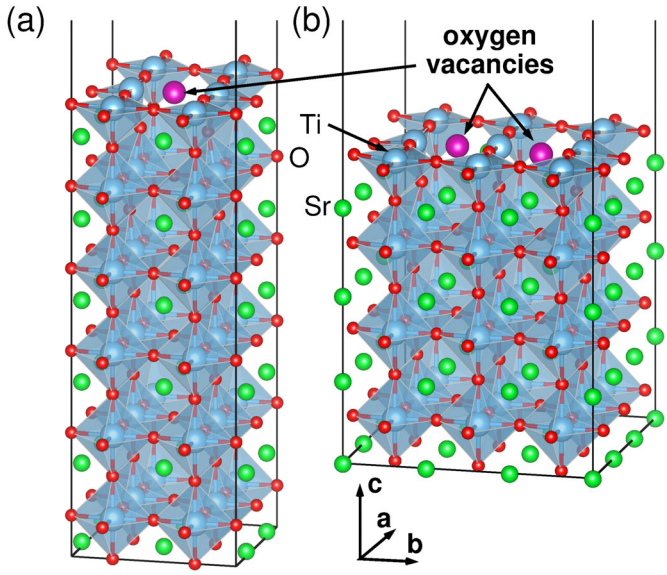

Fig. 1. Examples of single and double oxygen vacancy structures of $SrTiO_3$. (a) TiO_2 terminated $2 \times 2 \times 6$ slab with single vancancy in the surface layer. (b) TiO_2 terminated $3 \times 3 \times 4$ slab with two vacancies in the surface layer.

vacancy. The charge carriers, independently of the oxygen concentration, are strongly localized at the surface and deplete rapidly within a few layers from the surface, which indicates the formation of a two-dimensional electron system. Figure 2a shows the bandstructure near the Fermi level for the slab in Figure 1a where the extra electrons gained from the oxygen vacancy occupy Ti t_{2g} bands. The lowest narrow sub-bands are from in-plane Ti $3d_{xy}$ states predominantly localized on the surface TiO_2 layer and there are also shallow heavy bands of Ti $3d_{xz}$ character. These results agree well with ARPES experimental observations [1,2]. A closer look at the Fermi surface obtained with this slab (Fig. 2b) shows circular pockets around Γ of $3d_{xy}$ character and elliptical pockets of $3d_{xz}$ character with high effective masses along x and low effective masses along y. One should note that a defect in the TiO_2 layer breaks rotational symmetry and this is the reason why Figure 2b is not invariant under a rotation of 90°, however, in reality, surface oxygen defects are randomly distributed and a rotationally invariant Fermi surface is observed. Taking this into account, these results agree well with experiments.

The multivacancy cases disclose further interesting features. In our slab calculations we mainly focussed on two vacancies near a titanium dioxide terminated $SrTiO_3$ surface. Figure 3 shows the energy comparison for all slabs considered. The structure scheme to the right explains the color code of the symbols. The configuration of both vacancies in the first two layers (circles and triangles) is energetically clearly preferable to the cases of one or two layers separating the vacancies vertically (diamonds and pentagon). Concerning the lateral separation, 4 to 6 Å separation appears to be better than very short (2.5 Å) or very long (> 7 Å) distances between vacancies. One has to keep in mind though that the lateral size of the largest cell we could afford to study ($3 \times 3 \times 4$ supercell) is still rather small, and the issue of vacancy clustering could be reconsidered with larger computing power at some point.

Summarizing our observations, we conclude that the two vacancies preferably cluster vertically, inhabiting the first two layers, while in the direction parallel to the surface, the vacancies show a weak tendency towards equal spacing. Furthermore,

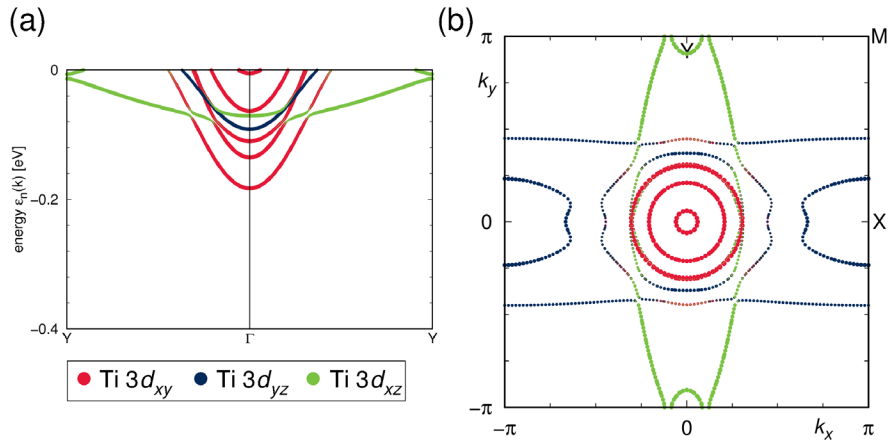

Fig. 2. (a) Band structure and (b) Fermi surface of a relaxed, TiO_2 terminated $2 \times 2 \times 6$ $SrTiO_3$ slab with a single vacancy in the TiO_2 surface layer (see Fig. 1a for the structure). This vacancy breaks the C_4 symmetry of the surface. Reprinted with permission from reference [5]. (This figure is subject to copyright protection and is not covered by a Creative Commons license.)

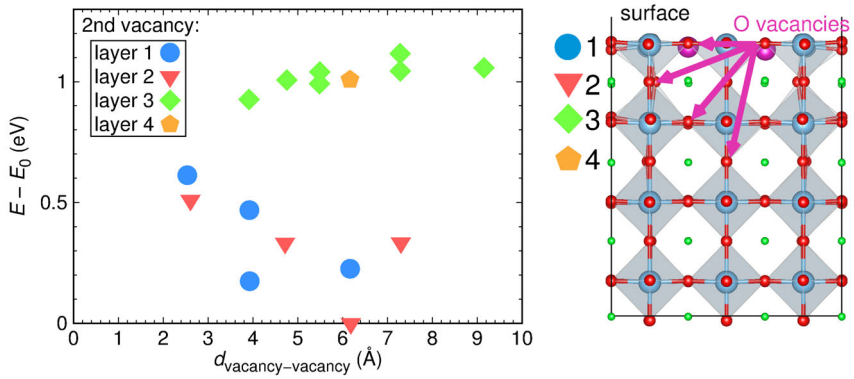

Fig. 3. Total energies of $SrTiO_3$ slabs with two oxygen vacancies calculated within GGA + U. The first vacancy is always in the surface TiO_2 layer (layer 1). Energies are given as function of distance to the second vacancy which can be in the surface TiO_2 layer (layer 1) (circles), in the subsurface SrO (layer 2) (triangles), in the first subsurface TiO_2 layer (layer 3) (diamonds) or in the second subsurface SrO layer (layer 4) (pentagon). Reprinted from reference [6].

analysis of the nonmagnetic electronic structure showed that oxygen defects in the surface TiO_2 layer lead to population of Ti t_{2g} states and thus itinerancy of the electrons donated by the oxygen vacancy. In contrast, electrons from subsurface oxygen vacancies populate Ti e_g states and remain localized on the two Ti ions neighboring the vacancy. We find that both the formation of a bound oxygen-vacancy state composed of hybridized Ti $3d$ e_g and $4p$ states neighboring the oxygen vacancy as well as the elastic deformation after extracting oxygen contribute to the stabilization of the in-gap states.

We finally analyze the effect of spin-orbit coupling and magnetism in $SrTiO_3$ slabs with oxygen vacancies. We performed fully relativistic nonmagnetic and magnetic density functional theory calculations [7] in the framework of the GGA + SO + U functional on representative oxygen deficient $SrTiO_3$ slabs and found clear signatures

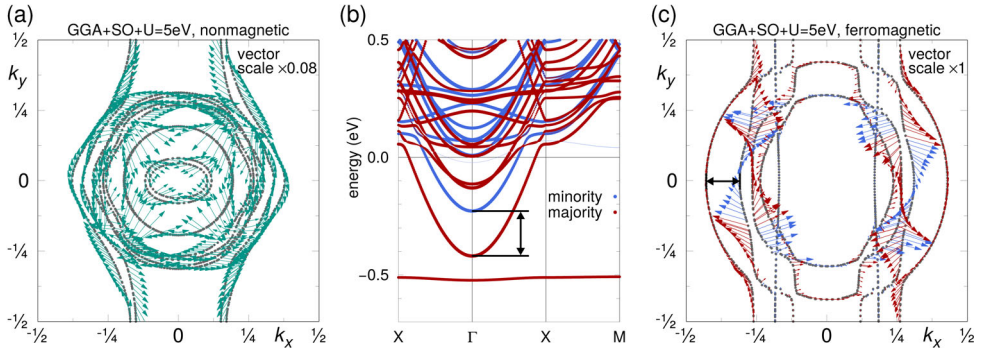

Fig. 4. Spin textures and spin-polarized band structures of a $3 \times 3 \times 4$ slab of $SrTiO_3$ with two oxygen vacancies (for the structure, see Fig. 1 b). (a) Nonmagnetic GGA+SO+U calculation with $U = 5\,\text{eV}$. (b) and (c) are ferromagnetic GGA+SO+U calculations with $m \parallel \hat{z}$. Reprinted with permission from reference [7]. (This figure is subject to copyright protection and is not covered by a Creative Commons license.)

of *atomic specialization*, namely, two types of electronic contributions: one is from Ti atoms neighboring the oxygen vacancies that acquire rather large magnetic moments and mostly create in-gap states; another comes from the partly polarized t_{2g} itinerant electrons of Ti atoms lying further away from the oxygen vacancy, which form the two-dimensional electron system and are responsible for Rashba spin winding and spin splitting at the Fermi surface.

In more detail, in agreement with the previous calculations above, Ti atoms neighboring the oxygen vacancies create e_g localized states that are responsible for the presence of in-gap states in the region of energies between -0.5 and $-1\,\text{eV}$ and the magnetic calculations show that they acquire large magnetic moments. In our simulations we found that the position of the in-gap states is influenced by the slab termination, the depth of the oxygen vacancy below the surface, and by possible oxygen clustering. Further, Ti atoms lying further away from the oxygen vacancy contribute with polarized t_{2g} itinerant electrons to the conducting 2DES and induce Rashba spin winding (see Fig. 4) and the spin splitting at the Fermi surface observed in SARPES [15]. Our calculations found that magnetism suppresses the Rashba effect by increasing the spin splitting of the t_{2g} orbitals and by modifying the individual spin orientation, but it does not eliminate completely spin winding as can be observed in the Fermi surface results for the $3 \times 3 \times 4$ slab of $SrTiO_3$ with two oxygen vacancies (compare Figs. 4a and 4c). Considering that an averaging of inhomogeneities near the surface of the measured sample is to be expected, SARPES measurements [15] could be explained by our calculations as the combined effect of the Rashba effect and magnetism.

2.2 Realistic DMFT for the oxygen-deficient $SrTiO_3$ surface

So far we discussed the electronic structure of the oxygen-deficient surface of $SrTiO_3$ as described within the DFT+U approach. Though that theoretical framework seems to provide good results for the present problem, one should be aware of its limitations. The effective single-particle DFT + U method describes electron correlations, based on local Coulomb interactions, in the static limit and is furthermore designed for long-range ordered phases. Several general aspects of Mott(-like) physics such as fluctuating moments, or band narrowing and spectral-weight transfer to Hubbard bands are missing.

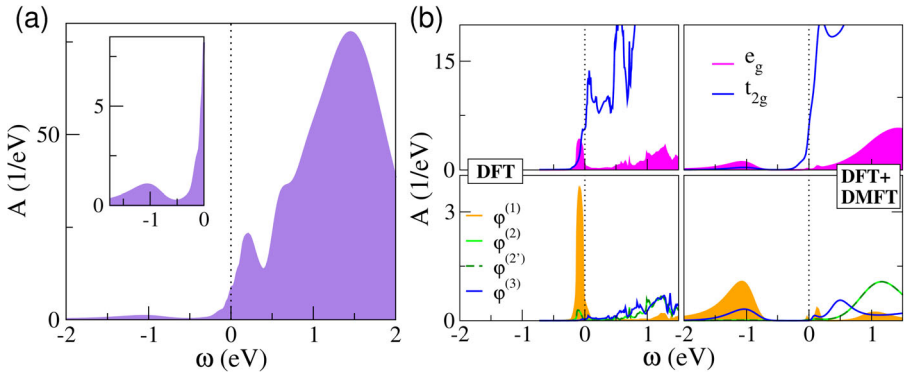

Fig. 5. DFT + DMFT results for an oxygen double vacancy on the $SrTiO_3$ surface. (a) Total spectral function. (b) Comparison of e_g vs. t_{2g} character (top) and spectra of selected local states with DFT results. Here $|\varphi^{(1)}\rangle \sim -0.33|z^2\rangle + 0.94|x^2 - y^2\rangle$ and $|\varphi^{(3)}\rangle \sim |yz\rangle$ are located on the Ti site embedded by the double vacancy, while $|\varphi^{(2,2')}\rangle \sim -0.39|z^2\rangle \pm 0.04|xz\rangle + 0.92|x^2 - y^2\rangle$ are next to both OVs.

We therefore advanced on the description of electronic correlations and applied the charge self-consistent merging of DFT with dynamical mean-field theory (DMFT) to the given surface defect problem [16]. Our approach [17] is here based on the combination of mixed-basis pseudopotential theory [18] for the DFT part and the continuous-time quantum Monte Carlo method [19,20], as implemented in the TRIQS package [21,22], for the DMFT impurity problem. In a slab supercell of 180 atomic sites, two structural oxygen-vacancy (OV) cases are investigated, namely a two-single-vacancies structure and a double-vacancy defect. The slab is structurally relaxed within DFT+U [6]. A Hubbard $U = 3.5\,\text{eV}$ and a Hund's exchange $J_\text{H} = 0.5\,\text{eV}$ are active on each Ti site, with a local correlated subspace of three effective $3d$ orbitals. There are 16 inequivalent Ti impurity problems in the supercell, and the coupled realistic problem is solved within multi-site DFT+DMFT at $T = 290\,\text{K}$ (see [16] for details).

In the following we restrict the discussion to the double-vacancy (DV) defect structure. Figure 5a displays the correlated paramagnetic spectral function with metallic character, with a pronounced in-gap weight at $\sim -1.2\,\text{eV}$. That location is in very good agreement with experimental findings [1,2,23–25]. The in-gap weight stems dominantly from localized Ti e_g orbitals near the defect, shifted to low energy because of a correlation-enhanced crystal field. Note that in conventional DFT, the defect-induced Ti e_g spectral weight remains close to the Fermi level, entwined with the onset of Ti t_{2g} weight from more delocalized states (see Fig. 5b). On the other hand, electronic correlations drive an obvious dichotomy, i.e., localized e_g far from the Fermi level and itinerant t_{2g} at low energy. Note that there still is some minor satellite-like t_{2g} character contributing to the in-gap peak, but a standard Mott-Hubbard picture does not apply.

2.3 Realistic DMFT for the oxygen-deficient $SrVO_3$

The previous sections showed that introduction of vacancies in $SrTiO_3$ forms both in-gap states and a 2DES at the surface of $SrTiO_3$. Furthermore, electronic correlations beyond conventional DFT appear as a vital ingredient to sustain these features. From a broader perspective, the findings are then in place to challenge the two customary paradigms in view of coexisting low- and high-energy electron states in condensed

matter. Namely, on the one side the weak-coupling defect-state picture from traditional semiconductor physics, and the strong-coupling Hubbard-band picture from traditional correlated-oxide physics on the other side. In the case of band-insulating $SrTiO_3$, commonly understood as being located close to a weak-coupling limit, it was here shown that strong correlation effects are indispensable to account for a proper description of oxygen-vacancy induced electronic states, albeit a conventional strong-coupling picture does not readily apply. Yet it is then tempting to choose another oxide system, by now commonly understood to reside close to that latter limit, and ask the question if oxygen vacancies are also effective in scrutinizing the other well-known paradigm, i.e., the Hubbard-band picture. For this purpose, the moderately correlated $SrVO_3$ serves as an ideal comparing materials test case, since it has the identical $SrTiO_3$ perovskite crystal structure and displays t_{2g}-based conductivity.

The $SrVO_3$ compound has been the *drosophila* model system to test the predictions of strongly correlated electron theories because it displays both coherent quasiparticles as well as incoherent excitations. This behaviour has been intensively studied both experimentally by angle resolved photoemission [26–28] and theoretically by a combination of density functional theory with dynamical mean field theory [29–31] and its extensions [32,33]. At a binding energy of about $-1.5\,\mathrm{eV}$, the angle integrated photoemission spectra of $SrVO_3$ show a broad peak that is usually interpreted as an incoherent excitation, a Hubbard band linked to the V t_{2g} electrons. However, a broad feature at about $-1.5\,\mathrm{eV}$ has been seen also in $SrTiO_3$, a $3d^0$ transition metal oxide where this feature has been clearly linked to the presence of oxygen defects as described above.

We have addressed this issue by performing charge selfconsistent DFT + DMFT calculations for example structures of $SrVO_3$ with oxygen vacancies; here we focus on the two vacancy case shown in the inset of Figure 6b. We chose values of $U = 2.5\,\mathrm{eV}$ and $J = 0.6\,\mathrm{eV}$ for vanadium. We compare k-integrated and k-resolved spectral functions (Fig. 6b and d) to bulk $SrVO_3$ without vacancies (Fig. 6a and c). While in the case of defect free $SrVO_3$, a t_{2g} quasiparticle peak at the Fermi level and a lower Hubbard band (LHB) at negative energies of the same t_{2g} nature is found in agreement with the ARPES result [34], the oxygen vacancies produce a dispersionless in-gap state at $\sim -1\,\mathrm{eV}$ which is of e_g character as in $SrTiO_3$. This is in very good agreement with the oxygen vacancy states observed in ARPES which are created by UV or X-ray irradiation. It means that the increase in intensity of the in-gap state in the oxygen-deficient $SrVO_3$ should not be attributed to an increase in population of the lower Hubbard satellite, but instead to the manifestation of vacancy states of e_g character.

2.4 Control of separate electronic phases

Electronic phase separation is a key concept in the field of many-body physics, in particular in the context of strongly correlated transition metal oxides [36]. It denotes a spatial inhomogeneity of the electronic and magnetic properties of a material at its surfaces, interfaces with other materials or in its bulk on the nano- to mesoscale. In a strict sense, it is induced in a chemically homogeneous solid when competing internal or mutual interactions between the charge, spin, orbit, and lattice degrees of freedom happen to depend strongly on electron density. Examples for such interactions include the superconducting pairing interaction, magnetic exchange or Rashba spin-orbit coupling [36,37].

The tendency to enhance locally the electron concentration in order to benefit in turn from the energy lowering of a given interaction is counteracted — or frustrated — by the Coulomb repulsion, leading to static or dynamic density fluctuations on

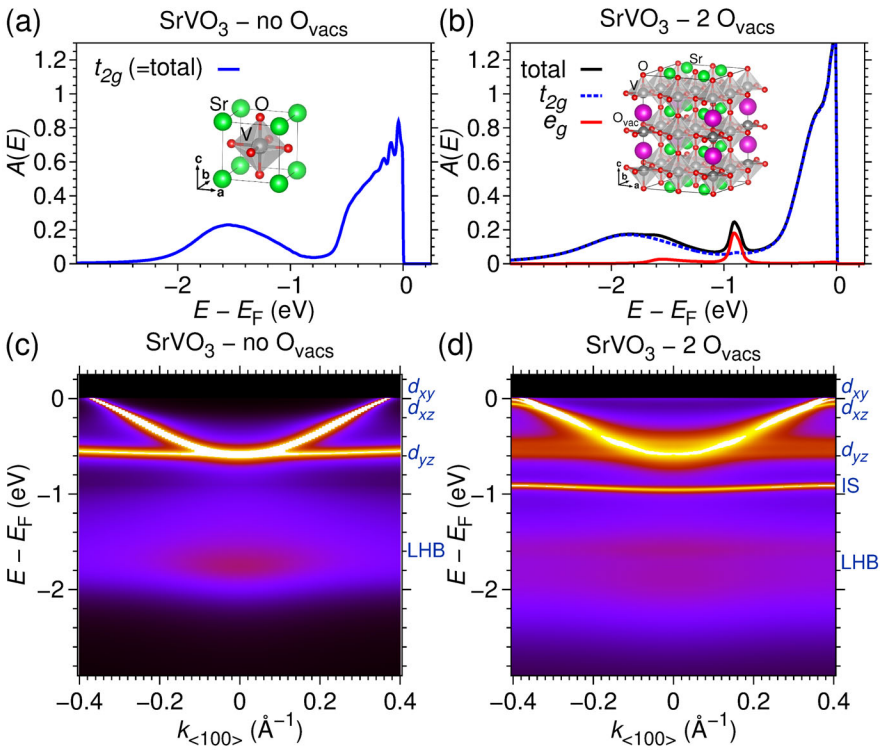

Fig. 6. LDA + DMFT results for $SrVO_3$, taking the renormalization of the bandwidth into account [35]. (a) k-integrated spectral function for bulk $SrVO_3$. A quasiparticle peak at E_F and a lower Hubbard band at -1.6 eV is seen in the V t_{2g} orbitals. (b) Spectral function for the $2 \times 2 \times 3$ supercell of $SrVO_3$ with two oxygen vacancies. An additional nondispersive V e_g vacancy state originating from the V atom neighboring the oxygen vacancies leads to a sharp peak below the Fermi level at ~ -1.0 eV. The V t_{2g} orbitals show a quasiparticle peak at E_F and a lower Hubbard band at -1.8 eV. (c,d) Show the corresponding spectral functions (multiplied by a $T = 20$ K Fermi-Dirac function) along the path $X - \Gamma - X$. Reprinted with permission from reference [34]. (This figure is subject to copyright protection and is not covered by a Creative Commons license.)

finite length scales [38,39]. These can be thought of being local precipitations of spatially homogeneous phases which exist in other portions of the phase diagram [40]. Famous material classes prone to electronic phase separation comprise manganites with their particular rich phase diagrams exhibiting metallic or insulating magnetic as well as charge-ordered phases [40], cuprate high-temperature superconductors displaying various types of intertwined order [41,42], but also less correlated Fe-based superconductors [43,44].

In a broader sense, the term electronic phase separation is used whenever two or more phases with differing electronic or magnetic properties coexist on microscopic length scales, including cases where the electronic phase separation is driven by inhomogeneities of the chemical composition or structural disorder [45,46].

Regarding $SrTiO_3$-based interfaces and surfaces Ariando et al. [47] were the first to report on electronic phase separation at the $LaAlO_3/SrTiO_3$ interface, i.e., in the region of the two-dimensional electron system. From electrical and magneto-transport data as well as magnetization measurements they inferred a separation of interface charges into dense nanoscopic droplets with a large diamagnetic moment below 60 K, ferromagnetic regions of about the same extension up to room temperature, and a

background quasi-two-dimensional electron gas. The occurrence and coexistence of these phases were found to depend strongly on growth conditions during pulsed laser deposition, though no specific microscopic scenario for the electronic phase separation was put forward.

Shortly after, Li et al. [48] and Bert et al. [49] communicated high-resolution magnetic torque magnetometry and direct imaging by scanning SQUID measurements, respectively, indicating the coexistence of ferromagnetism and superconductivity at the $LaAlO_3/SrTiO_3$ interface. As possible microscopic origin Li et al. suggested a non-uniform distribution of oxygen vacancies in the interfacial TiO_2 layers, stabilizing magnetic order of the Ti ions at the interface. Such a scenario would imply chemically driven electronic phase separation. From second harmonic generation Günter et al. [50] got evidence for spatial inhomogeneities at the $LaAlO_3/SrTiO_3$ interface on a length scale of $\approx 30\,\mu$m for film thicknesses not larger than a monolayer. In this study electronic effects were favoured over chemical ones, with clustering of oxygen defects being explicitly discarded.

Stimulated by the experimental observations theoretical work related to electronic phase separation at oxide interfaces was performed by Nanda and Satpathy [51], Caprara et al. [52], Pavlenko et al. [53], Bucheli et al. [54], Bovenzi et al. [37], Seibold et al. [55], and Scopigno et al. [56]. These studies draw up scenarios which are specific to oxide surfaces and interfaces to varying degrees and comprise mechanisms involving electron-phonon coupling [51], Rashba spin-orbit coupling [37,52,54,55], oxygen vacancies [53], the superconducting pairing interaction [37], and the electrostatic confinement potential at the interface [37,56].

Our own experimental work [57] in this context focused on the role of oxygen vacancies for the formation of a two-dimensional electron system at the surface of bare $SrTiO_3$ in (100) and (111) orientation. Using (angle-resolved) photoemission we got evidence for two separate electronic phases at the surface that are distinguished by a strong disproportionation of charge with respect to each other. We argue that a highly doped metallic phase is due to surface regions with a large oxygen vacancy concentration that are embedded in another insulating or only lightly electron-doped phase. Since oxygen vacancies are known to trap electrons at nearby Ti sites it is conceivable to relate the highly doped, oxygen vacancy rich phase to the ferromagnetic domains that were observed at the $LaAlO_3/SrTiO_3$ interface [48,49]. The other phase gets (additionally) doped in case of the heterointerface due to the polar discontinuity caused at the interface by the polar $LaAlO_3$ film on the non-polar $SrTiO_3$ substrate in order to compensate the arising electrostatic potential across the film.

To control the average oxygen vacancy concentration at the $SrTiO_3$ surface we employed a newly developed technique. On the one hand, oxygen vacancies are created under intense irradiation with X-rays at a synchrotron radiation facility [58]. On the other hand, a metal capillary in front of the sample allows to direct a steady flow of oxygen onto the $SrTiO_3$ surface. Thereby, oxygen vacancies are annihilated and a certain concentration of oxygen vacancies can be adjusted in a dynamical equilibrium through the oxygen flow [57].

At maximum dosing oxygen vacancies can be suppressed completely and the $SrTiO_3$ surface is insulating. At finite oxygen vacancy concentrations a two-dimensional electron system develops [1,2]. The positively charged oxygen vacancies provide a confinement potential at the surface resulting in a downward bending of the Ti $3d$ t_{2g} conduction bands. At the same time the oxygen vacancies donate a certain fraction of electrons to these bands forming two-dimensional quantum well states while the remaining fraction stays localized at Ti sites adjacent to the oxygen vacancies [59] as discussed in Section 2.1.

In photoemission these two types of electrons — itinerant and trapped ones — show up in different ways. In the Ti $3p$ core-level spectra (see Fig. 7c) additional

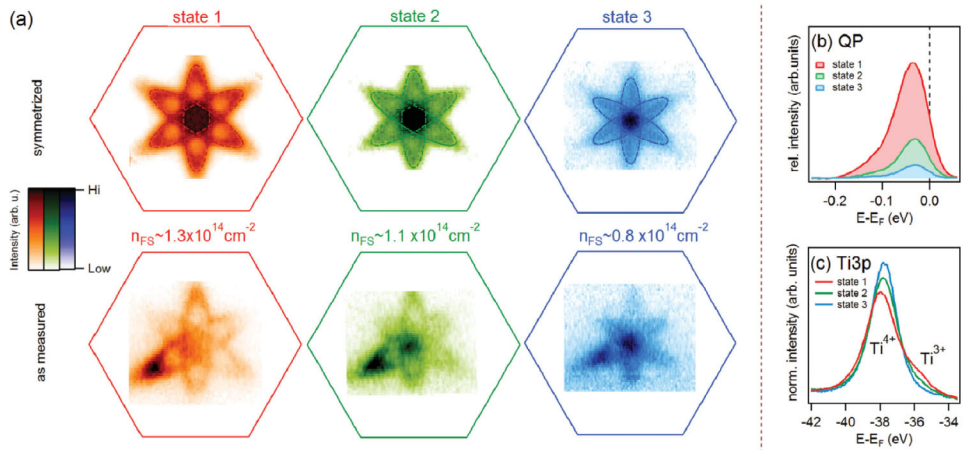

Fig. 7. (a) Fermi surface maps of the $SrTiO_3(111)$ surface for three states corresponding to different oxygen vacancy concentrations. Bottom row: as measured; top row: symmetrized. (b) k-integrated QP spectra. (c) Ti 3*p* core level spectra. For details see text. From reference [57]. (This figure is subject to copyright protection and is not covered by a Creative Commons license.)

electrons in the Ti 3*d* shell lead to emission at lower binding energies (Ti^{3+}) since an extra electron screens the core potential more effectively than in the case where Ti is in a 4+ oxidation state. Thus the Ti^{3+} emission is a measure of the total number of doped electrons. The itinerant electrons contributing to the metallic two-dimensional electron system give rise to a quasiparticle (QP) peak at the chemical potential (Fig. 7b). In a *k*-resolved (angle-resolved) photoemission measurement it corresponds to the three degenerate Ti 3*d* t_{2g} bands crossing the chemical potential and thus give rise to Fermi surface sheets as shown in Figure 7a for $SrTiO_3$ in (111) orientation (note that there are no indications for more than one occupied quantum well state in our data). According to Luttinger's theorem the Fermi surface area is a direct measure of the sheet carrier density of itinerant electrons, n_{FS}.

Evaluating n_{FS} from the Fermi surface sheets for three different states of a $SrTiO_3$ surface corresponding to three different oxygen vacancy concentrations gives only a moderate variation of the sheet carrier density between about $0.8 \times 10^{14}\,\mathrm{cm}^{-2}$ and $1.3 \times 10^{14}\,\mathrm{cm}^{-2}$. In contrast, the k-integrated QP intensity in Figure 7b shows a much stronger relative change in spectral weight for the same three states of the surface. This finding can be reconciled if one assumes the existence of a metallic phase A with only a slight increase of charge carrier density upon enhancing the oxygen vacancy concentration while its surface coverage rises strongly.

From the Ti^{3+}/Ti^{4+} ratio one can infer the sheet carrier density of the itinerant Ti 3*d* electrons averaged over the whole sampled surface area, n_{avg} (assuming a 1 : 1 disproportionation between localized and itinerant electrons due to the strong onsite Coulomb repulsion which prevents two electrons from being trapped at the same Ti site [59]). For a homogeneous distribution of charge carriers n_{avg} and n_{FS} would equal each other (blue line in Fig. 8 which plots these quantities against each other). However, as can be seen in Figure 8 n_{avg} is much smaller for the three prepared surface states, hinting again to the fact that there are highly doped metallic regions A embedded in an insulating or only lightly doped matrix B (see Fig. 8). With increasing coverage of the surface with phase A as can be read off from the QP intensity (right axis) the data points become closer to the blue line and are expected to fall onto it for a homogeneous coverage of the surface with phase A. The extrapolation of the

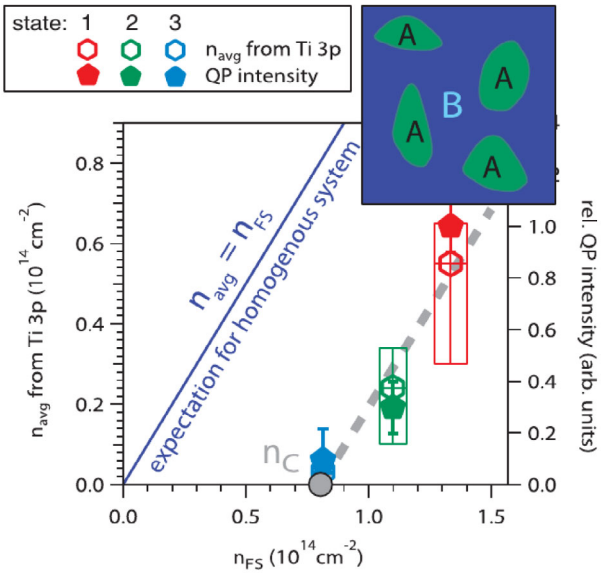

Fig. 8. Comparison of the sheet carrier densities for the three different states of Figure 7 as determined from the Fermi surface area (n_{FS}) and the Ti^{3+}/Ti^{4+} valence ratio in the Ti 3*p* spectra. Also plotted is the relative k-integrated QP intensity. For details see text. From reference [57]. (This figure is subject to copyright protection and is not covered by a Creative Commons license.)

data points in Figure 7 to zero average carrier density suggests that there is a certain critical electron density n_C for this phase to form.

Our findings for the bare $SrTiO_3$ surface are reminiscent of the electron phase separation in $LaAlO_3/SrTiO_3$, *viz.* the coexistence of ferromagnetic puddles embedded in a metallic (superconducting) matrix, mentioned above. They show that the $SrTiO_3$ surface or interface is prone to a non-uniform distribution of oxygen vacancies, giving rise to highly doped metallic regions. These then would correspond to the ferromagnetic puddles at the $LaAlO_3/SrTiO_3$ interface, with the local moments of trapped electrons aligning ferromagnetically. In this scenario we further identify the metallic matrix at the heterointerface with phase B, becoming (additionally) electron doped by the polar discontinuity at the interface. The electronic phase separation at the $LaAlO_3/SrTiO_3$ interface thus appears to be of chemical origin.

3 Two-dimensional electron systems at $SrTiO_3$-based heterointerfaces

3.1 Generic and specific doping mechanisms

Since the discovery of a two-dimensional electron system at the interface between the wide-gap band insulators $LaAlO_3$ and $SrTiO_3$ by Ohtomo and Hwang [60] numerous studies tried to pin down the exact mechanism leading to the formation of a conducting interface. It was found that the electron system forms only at and beyond a critical film thickness of 4 unit cells (uc) [61] and if the film is grown on TiO_2-terminated substrates. As a generic explanation electronic reconstruction was proposed [60,62]. In this scenario the potential build-up across the $LaAlO_3$ film due to the polar discontinuity at the interface — $SrTiO_3$ is unpolar while $LaAlO_3$ exhibits a stacking sequence of positively and negatively charged lattice planes — is compensated by the

transfer of half an electron from the $LaAlO_3$ surface into Ti 3*d* states at the interface. From tunnelling and capacity measurements Singh-Bhalla et al. [63] confirmed the existence of such a built-in potential. Also Reinle-Schmitt et al. [64] concluded on electronic reconstruction as origin of the conducting interface based on the observation that the critical thickness can be tuned by diluting $LaAlO_3$ with $SrTiO_3$, thereby changing the polar nature of the film. Similar conclusions were arrived at from surface X-ray diffraction measurements [65], revealing an atomic rumpling in the $LaAlO_3$ film due to the built-in electric field and from the study of electrostrictive effects [66].

Alternatively, extrinsic effects were invoked to account for the observed conductivity. Oxygen vacancies in $SrTiO_3$ donate itinerant electrons and could induce a metallic layer [67–69]. Likewise, cation intermixing at the interface, inherent to the growth process by pulsed laser deposition, would result in electron doping [70]. Finally, the role of adsorbates as charge reservoir for the interfacial electron system was pointed out in several studies [71–73].

Liu et al. [74] investigated the electric transport properties of $SrTiO_3$ substrates with crystalline and amorphous $LaAlO_3$ overlayers [75] and systematically changed parameters like film thickness or oxygen vacancy concentration. From their extensive studies Liu et al. arrived at the conclusion that oxygen vacancies are the dominant source of electrons when the film is amorphous whereas solely electronic reconstruction accounts for the conductivity in oxygen-annealed crystalline heterostructures where oxygen vacancies are completely suppressed.

From the above explanations only the electronic reconstruction scenario is able to naturally account for a critical thickness of the interfacial insulator-metal transition. Many theory papers reproduced the general picture, i.e., the band bending across the $LaAlO_3$ film with the concomitant shift of the valence band maximum towards and finally its crossing of the chemical potential at the critical thickness resulting in a charge transfer to the interface [76–78]. Other theoretical studies elucidated specific aspects of the electronic reconstruction scenario such as what actually leads to the confinement of the two-dimensional electron system [79,80] or why the experimentally determined sheet carrier densities [61] are an order of magnitude lower than one would expect from the transfer of half an electron to the interface [81,82].

The electronic reconstruction scenario, however, was also seriously cast into doubt by X-ray photoemission measurements providing a fairly sensitive probe for binding energy shifts — e.g., due to an internal electric field in the $LaAlO_3$ film — but being unable to reveal such traces of a finite potential gradient in the data [83–85]. Likewise, angle-resolved photoemission measurements using soft X-rays failed to observe O 2*p*-derived hole pockets due to the $LaAlO_3$ valence band Fermi level crossing as expected and predicted in an electronic reconstruction scenario [86].

Some theoretical studies provided an alternative view on the role of the polar discontinuity for the formation of the two-dimensional electron system taking defects, in particular oxygen vacancies, into account [71,78,87–90]. They pursue the idea that electronically active defects at the film surface like e.g., oxygen vacancies may serve as charge reservoir for the interfacial electron system. The electrons transferred to the interface together with the positively charged defect sites staying behind diminish the internal potential and may screen it out completely, resulting in flat bands across the film. Since the discharge energy per transferred electron increases with film thickness it will outweigh the defect formation energy at a certain critical value.

To shed light on the detailed mechanism at work behind the formation of a conducting interface and to clarify the nature of the two-dimensional electron system our own research [91] combined two approaches: (i) full control of the oxygen vacancy concentration in the $SrTiO_3$ substrate and simultaneous monitoring of the microscopic electronic structure at the chemical potential by photoemission as described

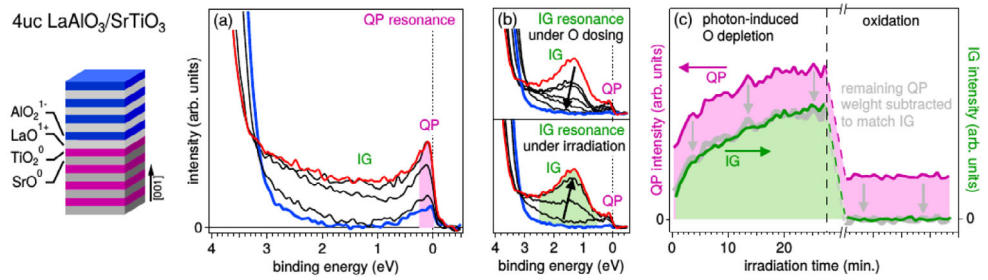

Fig. 9. Valence band spectra and evolution of QP and IG intensities of the metallic $LaAlO_3/SrTiO_3$ heterointerface with a 4 unit cell (uc) thick film for varying oxygen vacancy concentrations. (a) Evolution of heterostructure Ti *L*-edge resonant photoemission spectra under X-ray exposure, measured at the QP resonance. (b) Spectra measured at the IG resonance, solely under X-ray exposure (bottom) or under simultaneous oxygen dosing (top). The fully oxidized state is shown in blue, the one with saturated oxygen depletion in red. The black arrows indicate the direction of time. (c) QP (pink curve) and IG (green curve) spectral weights as function of X-ray exposure time with the oxygen dosing switched off and on. With the constant remaining QP spectral weight in the fully oxidized state of the heterostructure subtracted (grey curve), the QP spectral weight scales in direct proportion to that of the IG state. From reference [91]. (This figure is subject to copyright protection and is not covered by a Creative Commons license.)

in Section 2.4 and (ii) comparison of epitaxial and amorphous heterostructures to emulate the toggling of the polar discontinuity [74,75].

To overcome the small probing depth of conventional photoemission in the vacuum ultraviolet and to gain direct access to the electronic structure of the buried interface photoemission measurements have to be conducted in resonance at the Ti *L* absorption edge around 460 eV as first demonstrated by Drera et al. [92]. Thereby, the emission of electrons from Ti 3*d* states is enhanced. Looking at such resonance spectra in Figures 9 and 10 two structures can be discerned. The one right at the chemical potential represents the so-called quasiparticle peak (QP) due to the itinerant carriers contributing to the two-dimensional interface electron system. The other structure appearing at about 1.3 eV binding energy within the pristine gap (IG states) of $SrTiO_3$ corresponds to the emission of electrons trapped at Ti sites by nearby oxygen vacancies [24,26] (cf. Sects. 2.1 and 2.2). The energies of maximal resonance enhancement for both structures are shifted by about 1 eV against each other.

The results of these resonant photoemission experiments are summarized in Figure 9 for epitaxial and in Figure 10 for amorphous heterostructures. In both cases the photon energy was adjusted such to maximize resonant enhancement either of the QP peak or IG state. Turning first to the spectra of epitaxial $LaAlO_3/SrTiO_3$ it is seen that both QP and IG states grow in intensity under irradiation with X-rays (see Fig. 9b, bottom). The spectral changes are fully reversible under oxygen dosing using a metal capillary in front of the sample (see Fig. 9b, top). The red curves correspond to the state of saturated oxygen depletion reached in the experiment while the blue spectra represent the measurements with strongest oxygen dosing. Since essentially no IG weight is observed even under favourable resonance conditions for strongest oxygen dosing we consider this state as fully oxidized. Strikingly, as is better seen from the spectra displayed in Figure 9a, a QP component with finite weight remains under these conditions, while the IG states are completely suppressed.

A quantitative account of the QP and IG spectral weights upon oxygen depletion and re-oxidation is shown in Figure 9c. We plot them as obtained from integrating the photoemission spectra over the highlighted energy intervals in Figures 9a and 9b

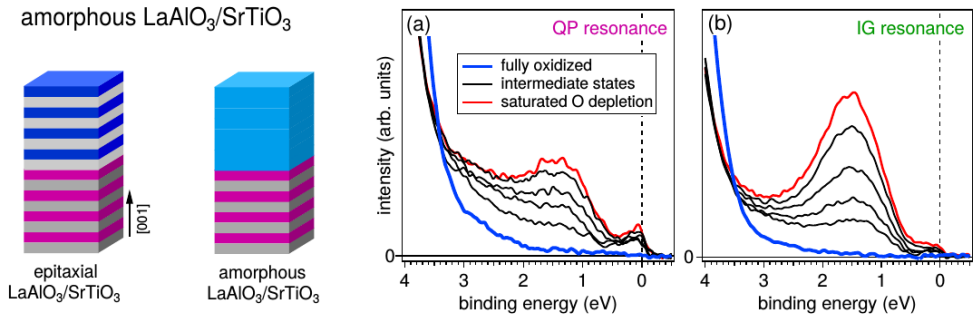

Fig. 10. Valence band spectra of an amorphous $LaAlO_3$ film for varying oxygen vacancy concentrations. Evolution of spectra for a 1.7 nm thick amorphous $LaAlO_3$ film under irradiation without oxygen dosing on the QP (a) and IG resonances (b). The fully oxidized state is shown in blue, the one with saturated oxygen depletion in red. From reference [91]. (This figure is subject to copyright protection and is not covered by a Creative Commons license.)

against X-ray irradiation time. The graph clearly displays the stationary finite weight of the QP peak after the fully oxidized state is accomplished while at the same time the IG weight vanishes. With this finite value subtracted, the rising curves of QP peak and IG state during irradiation induced depletion fall on top of each other indicating that the two electrons released per oxygen vacancy become itinerant or localized in a fixed — most likely 1 : 1 (see Sect. 2.4) — proportion.

It is instructive to compare these findings with similar measurements for an amorphous heterostructure with a 1.7 nm thick $LaAlO_3$ film (see Fig. 10), in which the polarity is lifted. Both features, QP and IG states, show a similar behaviour upon oxygen depletion (blue to red spectra) but with the salient difference that in the fully oxidized state also the QP peak gets fully suppressed.

This result of our dosing experiments clearly manifests the existence of a generic mechanism for the formation of a conducting interface in crystalline $LaAlO_3/SrTiO_3$ that is distinctly different from simple doping by oxygen vacancies as is realized at the interface of amorphous heterostructures. A persistent QP component even under full oxidation apparently requires not only the presence of a $LaAlO_3$ film but also its crystallinity, i.e., polar order. Our results thus tip the balance in favour of polar discontinuity as driving force for the intrinsic two-dimensional electron system. In the light of other photoemission studies cited above that could not pin down the existence of a built-in potential in the $LaAlO_3$ overlayer, the findings presented here are furthermore in support of proposals considering electronically active defects as crucial to understand the development of a conducting interface in epitaxial $LaAlO_3/SrTiO_3$ heterostructures.

3.2 Realistic DMFT and real-space model study of oxygen vacancies in the $LaAlO_3/SrTiO_3$ interface

As for the $SrTiO_3$ surface, first-principles studies of defect-induced physics in oxide interfaces are already challenging on the DFT(+U) level [78,88,93,94]. Averaged frameworks, like e.g., the virtual-crystal approximation, often miss relevant aspects of the spatial inhomogenity. But supercell approaches, due to size limitations and periodicity, usually only allow for high defect concentrations and impose artifical ordering patterns. Since an oxygen vacancy (OV) in $SrTiO_3$ singularly modifies the electronic structure on the local level, i.e., from Ti(d^0) towards Ti(d^1), we follow here a twofold supercell strategy to assess the dense and dilute defect cases. Realistic

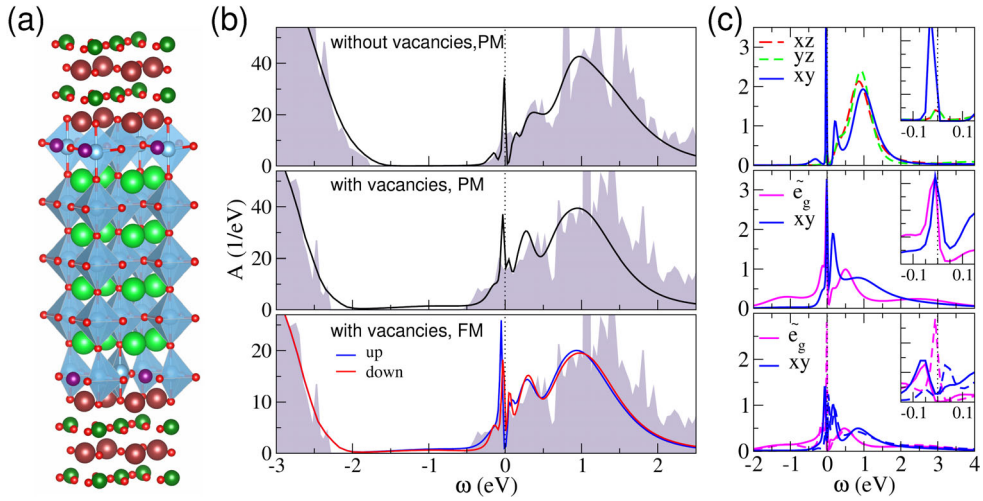

Fig. 11. DFT + DMFT study of oxygen-deficient $LaAlO_3/SrTiO_3$ ($U = 2.5\,\text{eV}$, $J_\text{H} = 0.5\,\text{eV}$, $T = 145\,\text{K}$). (a) Superlattice with Sr (large green), Ti (grey), O (small red), La (large dark red) and Al (small green) ions. (b) Total spectral function for different defect- and magnetic settings. Grey background marks the DFT(GGA) result. (c) Corresponding relevant local spectral functions to (b). Dashed lines in the bottom part mark the spin-down spectra.

superlattice DMFT calculations are performed for the dense defect limit [95] and a derived model Hamiltonian is applied to a large real-space lattice to treat the crossover to dilute defect scenarios [96].

Figure 11a shows the used inplane-doubled dense defect n-type supercell, with OVs in the TiO_2 layer right at the interface, whereby one out of four oxygen sites is vacant. Structural relaxations are handled on the DFT level within the generalized-gradient approximation (GGA). The system is already metallic without OVs due to the polar(-like) mechanism with close to 0.5 t_{2g} electrons on the interface Ti sites (cf. Fig. 11b). In the presence of OVs, the spectral function exhibits again in-gap weight of strong e_g kind around -1.2 eV [86,97–99], but now with a substantial Hubbard-band signature. That strong-correlation character might be partly related to the high defect concentration, enforcing nearly exactly d^1 occupation in the interface TiO_2 layer. More detailed comparing investigations to the findings on the $SrTiO_3$ surface are needed. Note that oxygen vacancies *and* correlations are essential to stabilize ferromagnetism in the $LaAlO_3/SrTiO_3$ interface.

The first-principles point of view renders it possible to utilize effective (e_g,t_{2g}) modellings [53,96]. We derived a minimal two-orbital model, consisting of a $t_{2g}(xy)$ state and an effective e_g state, i.e., $\tilde{e}_g$ [96]. The latter is lowered by crystal-field effects *if* an OV is adjacent. This model is solved with an efficient rotational-invariant slave-boson scheme [100,101] for differenct OV concentrations on a 10×10 TiO_2 interface lattice, whereby the explicit electronic oxygen degrees of freedom are integrated out. Intricate correlation-induced orbital polarizations with obvious differences close to and far from the defects are encountered. Magnetic ordering most notably changes from RKKY-like ferromagnetic (FM) order in the dilute defect case to local antiferromagnetism at intermediate concentrations, to finally a more robust double-exachange-driven FM state near the dense defect limit. This theoretical result allows one to trace the experimental observations of strongly varying Curie temperatures in different materials samples [47,102–104] to likely differences in the OV content.

4 Conclusions

In this review we have surveyed the influence of oxygen vacancies on the two-dimensional electron systems that are hosted at $SrTiO_3$-based interfaces and surfaces. The manifold of phenomena driven by oxygen defects is surprisingly rich. It comprises among others charge localization and doping, electronic phase separation, and correlation effects. Only advanced theoretical methods and computational schemes based on density functional as well as dynamical mean-field theory together with sophisticated experiments such as (high-energy) photoemission providing direct access to the microscopic electronic structure will advance the profound understanding of the underlying mechanisms with the perspective to utilize them in future devices and applications.

Support of the Deutsche Forschungsgemeinschaft through FOR 1346 is gratefully acknowledged.

References

1. A.F. Santander-Syro, O. Copie, T. Kondo, F. Fortuna, S. Pailhes, R. Weht, X.G. Qiu, F. Bertran, A. Nicolaou, A. Taleb-Ibrahimi, P. Le Fevre, G. Herranz, M. Bibes, N. Reyren, Y. Apertet, P. Lecoeur, A. Barthelemy, M.J. Rozenberg, Nature **469**, 189 (2011)
2. W. Meevasana, P.D.C. King, R.H. He, S-K. Mo, M. Hashimoto, A. Tamai, P. Songsiriritthigul, F. Baumberger, Z-X. Shen, Nat. Mater. **10**, 114 (2011)
3. C. Mitra, C. Lin, J. Robertson, A.A. Demkov, Phys. Rev. B **86**, 155105 (2012)
4. C. Lin, A.A. Demkov, Phys. Rev. Lett. **111**, 217601 (2013)
5. J. Shen, H. Lee, R. Valentí, H.O. Jeschke, Phys. Rev. B **86**, 195119 (2012)
6. H.O. Jeschke, J. Shen, R. Valentí, New J. Phys. **17**, 023034 (2015)
7. M. Altmeyer, H.O. Jeschke, O. Hijano-Cubelos, C. Martins, F. Lechermann, K. Koepernik, A. Santander-Syro, M.J. Rozenberg, R. Valentí, M. Gabay, Phys. Rev. Lett. **116**, 157203 (2016)
8. P.E. Blöchl, Phys. Rev. B **50**, 17953 (1994)
9. G. Kresse, J. Furthmüller, Comp. Mater. Sci. **6**, 15 (1996)
10. J. Hafner, J. Comp. Chem. **29**, 2044 (2008)
11. J.P. Perdew, K. Burke, M. Ernzerhof, Phys. Rev. Lett. **77**, 3865 (1996)
12. S.L. Dudarev, G.A. Botton, S.Y. Savrasov, C.J. Humphreys, A.P. Sutton, Phys. Rev. B **57**, 1505 (1998)
13. S. Okamoto, A.J. Millis, N.A. Spaldin, Phys. Rev. Lett. **97**, 056802 (2006)
14. K. Koepernik, H. Eschrig, Phys. Rev. B **59**, 1743 (1999)
15. A.F. Santander-Syro, F. Fortuna, C. Bareille, T.C. Roedel, G. Landolt, N.C. Plumb, J.H. Dil, M. Radovic, Nat. Mater. **13**, 1085 (2014)
16. F. Lechermann, H.O. Jeschke, A.J. Kim, S. Backes, R. Valentí, Phys. Rev. B **93**, 121103(R) (2016)
17. D. Grieger, C. Piefke, O.E. Peil, F. Lechermann, Phys. Rev. B **86**, 155121 (2012)
18. S.G. Louie, K.M. Ho, M.L. Cohen, Phys. Rev. B **19**, 1774 (1979)
19. A.N. Rubtsov, V.V. Savkin, A.I. Lichtenstein, Phys. Rev. B **72**, 035122 (2005)
20. P. Werner, A. Comanac, L.de' Medici, M. Troyer, A.J. Millis, Phys. Rev. Lett. **97**, 076405 (2006)
21. O. Parcollet, M. Ferrero, T. Ayral, H. Hafermann, I. Krivenko, L. Messio, P. Seth, Comput. Phys. Commun. **196**, 398 (2015)

22. P. Seth, I. Krivenko, M. Ferrero, O. Parcollet, Comput. Phys. Commun. **200**, 274 (2016)
23. H. Tanaka, T. Matsumoto, T. Kawai, S. Kawai, Jpn. J. Appl. Phys. **32**, 1405 (1993)
24. Y. Aiura, I. Hase, H. Bando, T. Yasue, T. Saitoh, D.S. Dessau, Surf. Sci. **515**, 61 (2002)
25. S. McKeown Walker, A. de la Torre, F.Y. Bruno, A. Tamai, T.K. Kim, M. Hoesch, M. Shi, M.S. Bahramy, P.C. King, F. Baumberger, Phys. Rev. Lett. **113**, 177601 (2014)
26. Y. Ishida, R. Eguchi, M. Matsunami, K. Horiba, M. Taguchi, A. Chainani, Y. Senba, H. Ohashi, H. Ohta, S. Shin, Phys. Rev. Lett. **100**, 056401 (2008)
27. T. Yoshida, M. Hashimoto, T. Takizawa, A. Fujimori, M. Kubota, K. Ono, H. Eisaki, Phys. Rev. B **82**, 085119 (2010)
28. S. Aizaki, T. Yoshida, K. Yoshimatsu, M. Takizawa, M. Minohara, S. Ideta, A. Fujimori, K. Gupta, P. Mahadevan, K. Horiba, H. Kumigashira, M. Oshima, Phys. Rev. Lett. **109**, 056401 (2012)
29. A. Sekiyama, H. Fujiwara, S. Imada, S. Suga, H. Eisaki, S.I. Uchida, K. Takegahara, H. Harima, Y. Saitoh, I.A. Nekrasov, G. Keller, D.E. Kondakov, A.V. Kozhevnikov, Th. Pruschke, K. Held, D. Vollhardt, V.I. Anisimov, Phys. Rev. Lett. **103**, 156402 (2004)
30. E. Pavarini, S. Biermann, A. Poteryaev, A.I. Lichtenstein, A. Georges, O.K. Andersen, Phys. Rev. Lett. **92**, 176403 (2004)
31. M. Aichhorn, L. Pourovskii, V. Vildosola, M. Ferrero, O. Parcollet, T. Miyake, A. Georges, S. Biermann, Phys. Rev. B **80**, 085101 (2009)
32. H. Lee, K. Foyevtsova, J. Ferber, M. Aichhorn, H.O. Jeschke, R. Valentí, Phys. Rev. B **85**, 165103 (2012)
33. J.M. Tomczak, M. Casula, T. Miyake, S. Biermann, Phys. Rev. B **90**, 165138 (2014)
34. S. Backes, T.C. Roedel, F. Fortuna, E. Frantzeskakis, P. Le Fevre, F. Bertran, M. Kobayashi, R. Yukawa, T. Mitsuhashi, M. Kitamura, K. Horiba, H. Kumigashira, R. Saint-Martin, A. Fouchet, B. Berini, Y. Dumont, A.J. Kim, F. Lechermann, H.O. Jeschke, M.J. Rozenberg, R. Valentí, A. F. Santander-Syro, Phys. Rev. B **94**, 241110(R) (2016)
35. M. Casula, Ph. Werner, L. Vaugier, F. Aryasetiawan, T. Miyake, A.J. Millis, S. Biermann, Phys. Rev. Lett. **109**, 126408 (2012)
36. E. Dagotto, Science **309**, 257 (2005)
37. N. Bovenzi, F. Finocchiaro, N. Scopigno, D. Bucheli, S. Caprara, G. Seibold, M. Grilli, J. Supercond. Nov. Magn. **28**, 1273 (2015)
38. V. Emery, S. Kivelson, Physica C **209**, 597 (1993)
39. J. Lorenzana, C. Castellani, C.D. Castro, Phys. Rev. B **64**, 235127 (2001)
40. E. Dagotto, *Nanoscale Phase Separation and Colossal Magnetoresistance*, Vol. 163 of Springer Series in Solid State Sciences (Springer, Berlin, Heidelberg, 2003)
41. R. Comin, R. Sutarto, E.H.da Silva Neto, L. Chauviere, R. Liang, W.N. Hardy, D.A. Bonn, F. He, G.A. Sawatzky, A. Damascelli, Science **347**, 1335 (2015)
42. E. Fradkin, S.A. Kivelson, J.M. Tranquada, Rev. Mod. Phys. **87**, 457 (2015)
43. J.T. Park, D.S. Inosov, C. Niedermayer, G.L. Sun, D. Haug, N.B. Christensen, R. Dinnebier, A.V. Boris, A.J. Drew, L. Schulz, et al., Phys. Rev. Lett. **102**, 117006 (2009)
44. A.O. Sboychakov, A.V. Rozhkov, K.I. Kugel, A.L. Rakhmanov, F. Nori, Phys. Rev. B **88**, 195142 (2013)
45. V. Moshnyaga, L. Sudheendra, O.I. Lebedev, S.A.Köster, K. Gehrke, O. Shapoval, A. Belenchuk, B. Damaschke, G.van Tendeloo, K. Samwer, Phys. Rev. Lett. **97**, 107205 (2006)
46. Y. Zhu, K. Du, J. Niu, L. Lin, W. Wei, H. Liu, H. Lin, K. Zhang, T. Yang, Y. Kou, et al., Nat. Commun. **7**, 11260 (2016)
47. Ariando, X. Wang, G. Baskaran, Z.Q. Liu, J. Huijben, J.B. Yi, A. Annadi, A. Roy Barman, A. Rusydi, S. Dhar, Y.P. Feng, J. Ding, H. Hilgenkamp, T. Venkatesan, Nat. Commun. **2**, 188 (2011)
48. L. Li, C. Richter, J. Mannhart, R.C. Ashoori, Nat. Phys. **7**, 762 (2011)
49. J.A. Bert, B. Kalisky, C. Bell, M. Kim, Y. Hikita, H.Y. Hwang, K.A. Moler, Nat. Phys. **7**, 767 (2011)

50. T.Günter, A. Rubano, D. Paparo, M. Lilienblum, L. Marrucci, F. Miletto Granozio, U. Scotti di Uccio, R. Jany, C. Richter, J. Mannhart, et al., Phys. Rev. B **86**, 235418 (2012)
51. B.R.K. Nanda, S. Satpathy, Phys. Rev. B **83**, 195114 (2011)
52. S. Caprara, F. Peronaci, M. Grilli, Phys. Rev. Lett. **109**, 196401 (2012)
53. N. Pavlenko, T. Kopp, J. Mannhart, Phys. Rev. B **88**, 201104(R) (2013)
54. D. Bucheli, M. Grilli, F. Peronaci, G. Seibold, S. Caprara, Phys. Rev. B **89**, 195448 (2014)
55. G. Seibold, S. Caprara, M. Grilli, R. Raimondi, EPL **112**, 17004 (2015)
56. N. Scopigno, D. Bucheli, S. Caprara, J. Biscaras, N. Bergeal, J. Lesueur, M. Grilli, Phys. Rev. Lett. **116**, 026804 (2016)
57. L. Dudy, M. Sing, P. Scheiderer, J.D. Denlinger, P. Schütz, J. Gabel, M. Buchwald, C. Schlueter, T.L. Lee, R. Claessen, Adv. Mater. **28**, 7443 (2016)
58. M.L. Knotek, P.J. Feibelman, Phys. Rev. Lett. **40**, 964 (1978)
59. C. Lin, A.A. Demkov, Phys. Rev. Lett. **113**, 157602 (2014)
60. A. Ohtomo, H.Y. Hwang, Nature **427**, 423 (2004)
61. S. Thiel, G. Hammerl, A. Schmehl, C.W. Schneider, J. Mannhart, Science **313**, 1942 (2006)
62. N. Nakagawa, H.Y. Hwang, D.A. Muller, Nat. Mater. **5**, 204 (2006)
63. G. Singh-Bhalla, C. Bell, J. Ravichandran, W. Siemons, Y. Hikita, S. Salahuddin, A.F. Hebard, H.Y. Hwang, R. Ramesh, Nat. Phys. **7**, 80 (2011)
64. M.L. Reinle-Schmitt, C. Cancellieri, D. Li, D. Fontaine, M. Medarde, E. Pomjakushina, C.W. Schneider, S. Gariglio, P. Ghosez, J.M. Triscone, et al., Nat. Commun. **3**, 932 (2012)
65. S.A. Pauli, S.J. Leake, B. Delley, M. Björck, C.W. Schneider, C.M. Schlepütz, D. Martoccia, S. Paetel, J. Mannhart, P.R. Willmott, Phys. Rev. Lett. **106**, 036101 (2011)
66. C. Cancellieri, D. Fontaine, S. Gariglio, N. Reyren, A.D. Caviglia, A. Fête, S.J. Leake, S.A. Pauli, P.R. Willmott, M. Stengel, et al., Phys. Rev. Lett. **107**, 056102 (2011)
67. A. Kalabukhov, R. Gunnarsson, J.Börjesson, E. Olsson, T. Claeson, D. Winkler, Phys. Rev. B **75**, 121404 (2007)
68. W. Siemons, G. Koster, H. Yamamoto, W.A. Harrison, G. Lucovsky, T.H. Geballe, D.H.A. Blank, M.R. Beasley, Phys. Rev. Lett. **98**, 196802 (2007)
69. G. Herranz, M. Basletić, M. Bibes, C. Carrétéro, E. Tafra, E. Jacquet, K. Bouzehouane, C. Deranlot, A. Hamzić, J.M. Broto, et al., Phys. Rev. Lett. **98**, 216803 (2007)
70. P.R. Willmott, S.A. Pauli, R. Herger, C.M. Schlepütz, D. Martoccia, B.D. Patterson, B. Delley, R. Clarke, D. Kumah, C. Cionca, et al., Phys. Rev. Lett. **99** (2007)
71. N.C. Bristowe, P.B. Littlewood, E. Artacho, Phys. Rev. B **83**, 205405 (2011)
72. Y. Xie, Y. Hikita, C. Bell, H.Y. Hwang, Nat. Commun. **2**, 494 (2011)
73. P. Scheiderer, F. Pfaff, J. Gabel, M. Kamp, M. Sing, R. Claessen, Phys. Rev. B **92**, 195422 (2015)
74. Z.Q. Liu, C.J. Li, W.M.Lü, X.H. Huang, Z. Huang, S.W. Zeng, X.P. Qiu, L.S. Huang, A. Annadi, J.S. Chen, et al., Phys. Rev. X **3** (2013)
75. Y. Chen, N. Pryds, J.E. Kleibeuker, G. Koster, J. Sun, E. Stamate, B. Shen, G. Rijnders, S. Linderoth, Nano Lett. **11**, 3774 (2011)
76. J. Lee, A.A. Demkov, Phys. Rev. B **78**, 193104 (2008)
77. W.j. Son, E. Cho, B. Lee, J. Lee, S. Han, Phys. Rev. B **79**, 245411 (2009)
78. Y. Li, S.N. Phattalung, S. Limpijumnong, J. Kim, J. Yu, Phys. Rev. B **84**, 245307 (2011)
79. K. Janicka, J.P. Velev, E.Y. Tsymbal, Phys. Rev. Lett. **102**, 106803 (2009)
80. P. Delugas, A. Filippetti, V. Fiorentini, D.I. Bilc, D. Fontaine, P. Ghosez, Phys. Rev. Lett. **106**, 166807 (2011)
81. Z.S. Popović, S. Satpathy, R.M. Martin, Phys. Rev. Lett. **101**, 256801 (2008)
82. R. Pentcheva, W.E. Pickett, Phys. Rev. Lett. **102**, 107602 (2009)
83. Y. Segal, J.H. Ngai, J.W. Reiner, F.J. Walker, C.H. Ahn, Phys. Rev. B **80**, 241107 (2009)

84. G. Berner, A.Müller, F. Pfaff, J. Walde, C. Richter, J. Mannhart, S. Thiess, A. Gloskovskii, W. Drube, M. Sing, et al., Phys. Rev. B **88**, 115111 (2013)
85. E. Slooten, Z. Zhong, H.J.A. Molegraaf, P.D. Eerkes, S. de Jong, F. Massee, E. van Heumen, M.K. Kruize, S. Wenderich, J.E. Kleibeuker, et al., Phys. Rev. B **87**, 085128 (2013)
86. G. Berner, M. Sing, H. Fujiwara, A. Yasui, Y. Saitoh, A. Yamasaki, Y. Nishitani, A. Sekiyama, N. Pavlenko, T. Kopp, C. Richter, J. Mannhart, S. Suga, , R. Claessen, Phys. Rev. Lett. **110**, 247601 (2013)
87. Z. Zhong, P.X. Xu, P.J. Kelly, Phys. Rev. B **82**, 165127 (2010)
88. N. Pavlenko, T. Kopp, E.Y. Tsymbal, J. Mannhart, G.A. Sawatzky, Phys. Rev. B **86**, 064431 (2012)
89. N.C. Bristowe, P. Ghosez, P.B. Littlewood, E. Artacho, J. Phys.: Condens. Matter **26**, 143201 (2014)
90. L. Yu, A. Zunger, Nat. Commun. **5**, 5118 (2014)
91. J. Gabel, M. Zapf, P. Scheiderer, P. Schütz, L. Dudy, M. Stübinger, C. Schlueter, T.L. Lee, M. Sing, R. Claessen, Phys. Rev. B **95**, 195109 (2017)
92. G. Drera, F. Banfi, F.F. Canova, P. Borghetti, L. Sangaletti, F. Bondino, E. Magnano, J. Huijben, M. Huijben, G. Rijnders, et al., Appl. Phys. Lett. **98**, 052907 (2011)
93. R. Pentcheva, W.E. Pickett, Phys. Rev. B **74**, 035112 (2006)
94. K. Janicka, J.P. Velev, E.Y. Tsymbal, J. Appl. Phys **103**, 07B508 (2008)
95. F. Lechermann, L. Boehnke, D. Grieger, C. Piefke, Phys. Rev. B **90**, 085125 (2014)
96. M. Behrmann, F. Lechermann, Phys. Rev. B **92**, 125148 (2015)
97. K.-J. Zhou, M. Radovic, J. Schlappa, V. Strocov, R. Frison, J. Mesot, L. Patthey, T. Schmitt, Phys. Rev. B **83**, 201402(R) (2011)
98. Z. Ristic, R. DiCapua, F. Chiarella, G.M. DeLuca, I. Maggio-Aprile, M. Radovic, M. Salluzzo, Phys. Rev. B **86**, 045127 (2012)
99. C. Cancellieri, M.L. Reinle-Schmitt, M. Kobayashi, V.N. Strocov, T. Schmitt, P.R. Willmott, S. Gariglio, J.-M. Triscone, Phys. Rev. Lett. **110**, 137601 (2013)
100. F. Lechermann, A. Georges, G. Kotliar, O. Parcollet, Phys. Rev. B **76**, 155102 (2007)
101. T. Li, P.Wölfle, P.J. Hirschfeld, Phys. Rev. B **40**, 6817 (1989)
102. M.R. Fitzsimmons, N.W. Hengartner, S. Singh, M. Zhernenkov, F.Y. Bruno, J. Santamaria, A. Brinkman, M. Huijben, H.J.A. Molegraaf, J.de la Venta, , I.K. Schuller, Phys. Rev. Lett. **107**, 217201 (2011)
103. A. Ron, E. Maniv, D. Graf, J.-H. Park, Y. Dagan, Phys. Rev. Lett. **113**, 216801 (2014)
104. F. Bi, M. Huang, S. Ryu, H. Lee, C.-W. Bark, C.-B. Eom amd P. Irvin, J. Levy, Nat. Commun. **5**, 5019 (2014)